Phase-field model for binary alloys

Seong Gyoon Kim
RASOM and Department of Materials Science and Engineering, Kunsan National University, Kunsan 573-701, Korea

Won Tae Kim
Center for Noncrystalline Materials and Department of Physics, Chongju University, Chongju 360-764, Korea

Toshio Suzuki
Department of Materials Engineering, The University of Tokyo, Tokyo 113, Japan
(Received 17 March 1999; revised manuscript received 2 August 1999)

We present a phase-field model (PFM) for solidification in binary alloys, which is found from the phase-field model for a pure material by direct comparison of the variables for a pure material solidification and alloy solidification. The model appears to be equivalent with the Wheeler-Boettinger-McFadden (WBM) model [A.A. Wheeler, W. J. Boettinger, and G. B. McFadden, Phys. Rev. A **45**, 7424 (1992)], but has a different definition of the free energy density for interfacial region. An extra potential originated from the free energy density definition in the WBM model disappears in this model. At a dilute solution limit, the model is reduced to the Tiaden *et al.* model [Physica D **115**, 73 (1998)] for a binary alloy. A relationship between the phase-field mobility and the interface kinetics coefficient is derived at a thin-interface limit condition under an assumption of negligible diffusivity in the solid phase. For a dilute alloy, a steady-state solution of the concentration profile across the diffuse interface is obtained as a function of the interface velocity and the resultant partition coefficient is compared with the previous solute trapping model. For one dimensional steady-state solidification, where the classical sharp-interface model is exactly soluble, we perform numerical simulations of the phase-field model: At low interface velocity, the simulated results from the thin-interface PFM are in excellent agreement with the exact solutions. As the partition coefficient becomes close to unit at high interface velocities, whereas, the sharp-interface PFM yields the correct answer. [S1063-651X(99)08712-7]

PACS number(s): 64.70.Dv, 81.30.Fb, 81.10.Aj, 05.70.Ln

I. INTRODUCTION

The phase-field model (PFM) is known to be very powerful in describing the complex pattern evolution of the interface between mother and new phases in the nonequilibrium state because all the governing equations are written as unified ones in the whole space of system. The model which was originally proposed for simulating dendritic growth in pure undercooled melt [1–9] has been extended to solidification modeling of alloys [10–20].

The PFMs for alloy solidification may be divided into three groups depending on the definition of free energy density for interfacial region and how they were derived: The first is a model by Wheeler, Boettinger, and McFadden (WBM) model [10,13]. Caginalp and Xie [16] have proposed a similar model. The second is a model by Steinbach *et al.* [17,18] The thirds are the models by Losert *et al.* [19], and Löwen, Bechhoefer, and Tuckerman [20], which are analogical versions of the PFM of pure materials.

The WBM model that has been used most widely [10,11,13,21,22] is derived in a thermodynamically consistent way [13]. In the model, any point within the interfacial region is assumed to be a mixture of solid and liquid both with the same composition. The phase field parameters in the model can be determined not only at a sharp interface limit condition [10], but also at a finite interface thickness condition [23]. It has been shown that the model can reproduce correctly the solute trapping phenomena at a high interface velocity [21–23]. A problem in this model, especially in numerical simulation where a finite interface thickness is assumed, is the parameters varying depending on the interface thickness [23]. Due to chemical energy contribution to the interfacial energy, there is a certain limit in the interface thickness, which is not only restricted by the interface energy, but also the difference between the equilibrium liquid and solid compositions.

The model by Steinbach and co-workers [17,18] uses a different definition for the free energy density. In the model, the interfacial region is assumed to be a mixture of solid and liquid with different compositions, but constant in their ratio. Even though the derivation of governing equations in the model was not made in a thermodynamically consistent way, there is no limit in the interface thickness. The model is thermodynamically correct for a dilute alloy only.

It has long been realized that the governing equations describing alloy solidification are similar to the ones corresponding to pure material [24]. This enables us to extend straightforwardly the PFM for a pure material to an alloy PFM, by matching the variables in the pure material problem to the alloy problem. In this way, Losert *et al.* [19] extended the thin-interface PFM for a pure material to an alloy case, which permits us to find vanishing interface kinetics coefficient. However, their model is based on two unrealistic assumptions: First the liquidus and solidus lines in the phase diagram were assumed to be parallel and secondly the solute diffusivity is constant in the whole space of the system. In

general, the slopes of liquidus and solidus lines in the phase diagrams of most alloys are significantly different from each other and the diffusivity in solid phase is much smaller than that in liquid phase by about orders of 5.

In this study, we present an alloy PFM and describe its properties in detail. The model is a natural extension of the PFM for pure materials and may also be derived in a thermodynamically consistent way. The model is free from the limit in the interface thickness in the WBM model [10,13], and the unrealistic assumptions in the Losert *et al.* model [19], and correctly generates the solute trapping phenomena at high interface velocity. In Sec. II, by reexamining the correspondence between the variables in the sharp interface model of pure material solidification and alloy solidification, we find an alloy PFM from a pure material PFM. It will also be shown that the model is equivalent to the WBM model [10,13], only with a different definition of the free energy density for the interfacial region. Also it will be shown that in a very dilute solution the present model can be reduced to the Steinbach and co-workers model [17,18] for a binary alloy. In Sec. III, a relationship between the phase-field mobility and the interface kinetics coefficient is derived at a thin-interface limit condition under an assumption of negligible diffusivity in solid phase, which permits not only a vanishing kinetics coefficient, but also a thick interface width, as in Refs. [25], [19]. In Sec. IV, for a dilute alloy, a steady-state solution of the concentration profile across the interface is derived as a function of the interface velocity and the resultant partition coefficient is compared with the high velocity asymptotics [22] of the WBM model. In Sec. V, at one-dimensional (1D) steady state where the classical sharp interface model is exactly soluble, we perform numerical simulations for the PFM with the parameters determined at the thin-interface limit (thin-interface PFM) and the sharp interface limit conditions (sharp-interface PFM).

II. ALLOY PHASE-FIELD MODEL

A. An alloy phase-field model

At first we examine the correspondence between variables in governing equations of pure material and alloy solidification in the classical sharp interface models. When the specific heats of solid and liquid are same and independent of temperature, the enthalpies per unit volume of solid and liquid of a pure material as a function of temperature are given by

$$H_S(T_S)=H_S(T_m)+c_p(T_S-T_m), \tag{1}$$

$$H_L(T_L)=H_L(T_m)+c_p(T_L-T_m), \tag{2}$$

respectively, where T_S and T_L are the temperatures of solid and liquid, respectively, T_m is the melting temperature of the pure material, and c_p is the specific heat. Then the classical sharp-interface model describing the solidification in a pure material may be written as

$$(H_S)_t=D_S^T\nabla^2 H_S, \tag{3}$$

$$(H_L)_t=D_L^T\nabla^2 H_L, \tag{4}$$

$$T_S^i=T_L^i=T_m-\frac{T_m}{\Delta H_f}\frac{2\sigma}{r}-\beta V, \tag{5}$$

$$(H_L^i-H_S^i)V=D_S^T\frac{\partial H_S}{\partial n}-D_L^T\frac{\partial H_L}{\partial n}, \tag{6}$$

where the subscript t and $\partial/\partial n$ mean the partial derivative by time and the interface normal derivative, respectively, D_S^T and D_L^T are thermal diffusivities of solid and liquid, respectively, the superscript i on temperature and enthalpy denotes the values at the interface, σ is the interface energy, r is the radius of the interface curvature, V is the interface velocity, β is the interface kinetics coefficient, and $\Delta H_f(=H_L^i-H_S^i)$ is the latent heat of melting. Equation (5) is the Gibbs-Thomson condition corrected by a kinetic undercooling effect and Eq. (6) is the energy balance condition at the interface. Using Eqs. (1) and (2), if the enthalpy notations in Eqs. (3), (4) and the right-hand side of Eq. (6) are replaced by the temperature notations, the above equations appear to be equivalent to the traditional forms. Now we write the classical sharp interface model for isothermal solidification of an alloy as

$$(c_S)_t=D_S\nabla^2 c_S, \tag{7}$$

$$(c_L)_t=D_L\nabla^2 c_L, \tag{8}$$

$$f_{c_S}^S(c_S^i)=f_{c_L}^L(c_L^i)=f_c^e-\frac{\Delta H_f}{T_m(c_L^e-c_S^e)}\beta V-\frac{2\sigma}{r(c_L^e-c_S^e)}, \tag{9}$$

$$(c_L^i-c_S^i)V=D_S\frac{\partial c_S}{\partial n}-D_L\frac{\partial c_L}{\partial n}, \tag{10}$$

where c_S and c_L are the compositions of solid and liquid, respectively, D_S and D_L are the diffusivities of solute in solid and liquid, respectively, c_S^i and c_L^i are the compositions of solid side and liquid side at the interface, respectively, c_S^e and c_L^e are the equilibrium compositions of solid and liquid at a given temperature, respectively, $f_{c_S}^S$ and $f_{c_L}^L$ are the chemical potential of solid and liquid, respectively, and f_c^e is the chemical potential at a thermodynamic equilibrium state. Hereafter the chemical potential denotes the relative chemical potential of solute with respect to solvent. By comparing Eqs. (7)–(10) with Eqs. (3)–(6), we can see that replacing the enthalpy and the temperature in the equations for a pure material by the composition and the chemical potential, respectively, yields the equations for isothermal solidification in an alloy. This correspondence between the variables may permit us to derive an alloy PFM from the PFM for a pure material.

Let us write the PFM for the solidification of a pure material, which is basically the same as the previously reported form [5–9], as follows:

$$H_t=\nabla\cdot k(\phi)\nabla T, \tag{11}$$

$$\phi_t=M(\epsilon^2\nabla^2\phi-f_\phi), \tag{12}$$

$$H=h(\phi)H_S+[1-h(\phi)]H_L, \tag{13}$$

$$T_S(x,t)=T_L(x,t)\equiv T(x,t), \tag{14}$$

$$f[H(T),\phi]=h(\phi)f^S[H_S(T_S)] + [1-h(\phi)]f^L[H_L(T_L)]+wg(\phi), \tag{15}$$

where we defined the phase field $\phi=1$ at solid and $\phi=0$ at liquid, $k(\phi)$ is the thermal conductivity, M is phase-field mobility, ϵ is the coefficient of phase-field gradient energy term in the relevant free energy functional, w is the height of the double-well potential, f^S and f^L are the free energy densities of solid and liquid as a function of temperature or enthalpy, respectively, and $g(\phi)$ is a double-well potential. The function $h(\phi)$ is a monotonously changing function from $h(0)=0$ to $h(1)=1$. In Eqs. (13)–(15) we should note that the interfacial region is assumed to be a mixture of solid and liquid with a same temperature. When H is eliminated by using Eqs. (1) and (2), Eqs. (11)–(15) can be reduced to only two equations

$$c_pT_t-\Delta H_f h'(\phi)\phi_t=\nabla\cdot k(\phi)\nabla T, \tag{16}$$

$$\phi_t=M[\epsilon^2\nabla^2\phi+h'(\phi)(f^L-f^S)-wg'(\phi)], \tag{17}$$

which are identical with those in the PFM for a pure material [5–9].

Using the correspondence between the variables in the classical sharp interface models for pure material and alloy solidification, that is, simply replacing H and T in Eqs. (11)–(15) by c and f_c, respectively, we can immediately write the equations for an alloy PFM as follows:

$$c_t=\nabla\cdot\frac{D(\phi)}{f_{cc}}\nabla f_c, \tag{18}$$

$$\phi_t=M(\epsilon^2\nabla^2\phi-f_\phi), \tag{19}$$

together with

$$c=h(\phi)c_S+[1-h(\phi)]c_L, \tag{20}$$

$$f^S_{c_S}[c_S(x,t)]=f^L_{c_L}[c_L(x,t)], \tag{21}$$

$$f(c,\phi)=h(\phi)f^S(c_S)+[1-h(\phi)]f^L(c_L)+wg(\phi), \tag{22}$$

where $D(\phi)$ is the diffusivity dependent on the phase field. f^S and f^L are the free energy densities of solid and liquid as functions of composition, which can be given either by a solution model of an alloy or thermodynamic data. In Eq. (18), f_{cc} was added to guarantee a constant diffusivities in both the bulk solid and liquid. The diffusion equation (18) and the phase-field equation (19) are the same as those in the WBM model [13], which were derived in a thermodynamically consistent way. In Eqs. (20)–(22), however, the interfacial region is defined as a mixture of solid and liquid with compositions different from each other, but with a same chemical potential. In the WBM model [10,13], on the contrary, the interfacial region was defined as a mixture of solid and liquid with a same composition, but with different chemical potentials. If the condition (21) is replaced by a condition $c_S=c_L=c$, the above model is reduced to the WBM model. Which definition for the interfacial region is more physically resonable does not matter, because the interfacial region in PFMs cannot be regarded as a physical real entity, but as a mathematical entity for technical convenience. It should be mentioned that c_S and c_L in Eqs. (20) and (21) are not the compositions of the solid and liquid sides of the interface, but the compositions of solid and liquid, respectively, at a certain infinitesimal point which is assumed to be a mixture of solid and liquid phases. Thus the condition (21) does not imply the constant chemical potential throughout the interfacial region. It is constant across the interface only at a thermodynamic equilibrium state, which will be shown later. The chemical potential can vary across the moving interface from the chemical potential at the solid side to the chemical potential at the liquid side of the interface, which results in the solute trapping effect [26–28]. In most alloys except for some specific (ideal or regular) solutions, the material properties such as interface energy and interface kinetics coefficient of an alloy are seldom derivable from the data of pure solvent and pure solute. In this case, the properties of the alloy can be given as constants in most cases. Therefore we assumed that the material properties are independent of the composition.

Equations (18) and (19) in the present model may be modified into more tractable forms described explicitly by c_S and c_L instead of c. Regarding c_S and c_L as functions of c and ϕ, from Eqs. (20) and (21) we can get following four relationships:

$$\frac{\partial c_L}{\partial c}=\frac{f^S_{cc}(c_S)}{[1-h(\phi)]f^S_{cc}(c_S)+h(\phi)f^L_{cc}(c_L)}, \tag{23}$$

$$\frac{\partial c_S}{\partial c}=\frac{f^L_{cc}(c_L)}{[1-h(\phi)]f^S_{cc}(c_S)+h(\phi)f^L_{cc}(c_L)}, \tag{24}$$

$$\frac{\partial c_L}{\partial \phi}=\frac{h'(\phi)(c_L-c_S)f^S_{cc}(c_S)}{[1-h(\phi)]f^S_{cc}(c_S)+h(\phi)f^L_{cc}(c_L)}, \tag{25}$$

$$\frac{\partial c_S}{\partial \phi}=\frac{h'(\phi)(c_L-c_S)f^L_{cc}(c_L)}{[1-h(\phi)]f^S_{cc}(c_S)+h(\phi)f^L_{cc}(c_L)}, \tag{26}$$

where we used the notations of $f^L_{cc}(c_L)\equiv d^2f^L(c_L)/dc_L^2$ and $f^S_{cc}(c_S)\equiv d^2f^S(c_S)/dc_S^2$. Using these four relationships, from the definition (22) of the free energy density we can derive

$$f_\phi(c,\phi)=-h'(\phi)\left[f^L(c_L)-f^S(c_S)-\frac{df^L(c_L)}{dc_L}(c_L-c_S)\right] + wg'(\phi), \tag{27}$$

$$f_c(c,\phi)=\frac{df^L(c_L)}{dc_L}=\frac{df^S(c_S)}{dc_S}, \tag{28}$$

$$f_{cc}(c,\phi)=\frac{f^S_{cc}(c_S)f^L_{cc}(c_L)}{[1-h(\phi)]f^S_{cc}(c_S)+h(\phi)f^L_{cc}(c_L)}, \tag{29}$$

$$\frac{f_{c\phi}(c,\phi)}{f_{cc}(c,\phi)}=h'(\phi)(c_L-c_S). \tag{30}$$

Inserting Eqs. (27) and (28) into Eqs. (18) and (19), we get the explicit forms of the present model:

$$\frac{1}{M}\phi_t=\nabla\cdot\epsilon^2\nabla\phi+h'(\phi)[f^L(c_L)-f^S(c_S)-(c_L-c_S)f^L_{c_L}(c_L)]-wg'(\phi), \tag{31}$$

$$\frac{\partial c}{\partial t}=\nabla\left[\frac{D(\phi)}{f_{cc}}\nabla f^L_{c_L}(c_L)\right] \tag{32}$$

together with auxiliary equations (20), (21), and (29). Using Eq. (30), the diffusion equation (32) may be expressed into an equivalent equation

$$\frac{\partial c}{\partial t}=\nabla[D(\phi)\nabla c]+\nabla[D(\phi)h'(\phi)(c_L-c_S)\nabla\phi]. \tag{33}$$

B. Dilute solution approximation

The dilute solution limit is often useful for both engineering applications and finding out fundamentals. Here we write full equations of the present model at the limit. Equation (21) yields

$$\frac{c^e_S c_L}{c^e_L c_S}=\frac{(1-c^e_S)(1-c_L)}{(1-c^e_L)(1-c_S)}, \tag{34}$$

where c^e_S and c^e_L are the equilibrium compositions of solid and liquid, respectively. Also we can get the following equations:

$$G(c_S,c_L)\equiv f^L(c_L)-f^S(c_S)-(c_L-c_S)f^L_{c_L}(c_L)=\frac{RT}{v_m}\ln\frac{(1-c^e_S)(1-c_L)}{(1-c^e_L)(1-c_S)}, \tag{35}$$

$$H(\phi,c_S,c_L)\equiv\frac{RT}{v_m f_{cc}}=[1-h(\phi)]c_L(1-c_L)+h(\phi)c_S(1-c_S), \tag{36}$$

$$f^L_{c_L}(c_L)=A+\frac{RT}{v_m}\ln\frac{c_L}{1-c_L}, \tag{37}$$

where v_m is the molar volume, R is the gas constant, and A in the last equation is a material's constant. Therefore we can write the phase-field and diffusion equations as

$$\frac{1}{M}\phi_t=\nabla\cdot\epsilon^2\nabla\phi+h'(\phi)G(c_S,c_L)-wg'(\phi), \tag{38}$$

$$c_t=\nabla\left[D(\phi)H(\phi,c_S,c_L)\nabla\ln\frac{c_L}{1-c_L}\right]. \tag{39}$$

The present model at the dilute solution limit consist of Eqs. (20), (34), (38), and (39).

It should be addressed that our model closly resembles the Steinbach *et al.* model [17,18]. With $h(\phi)=\phi$, the diffusion equation (33) becomes

$$\frac{\partial c}{\partial t}=\nabla[D(\phi)\nabla c]+\nabla[D(\phi)(c_L-c_S)\nabla\phi]. \tag{40}$$

At the limit where all compositions go to zero, Eq. (34) can be further approximated as

$$\frac{c_S}{c_L}=\frac{c^e_S}{c^e_L}=k^e, \tag{41}$$

where k^e is the equilibrium partition coefficient. With Eq. (41) we see

$$G(c_S,c_L)\simeq\frac{RT}{v_m}[(c^e_L-c^e_S)-(c_L-c_S)]=\frac{RT(1-k^e)}{v_m m^e}(T_m-T-m^e c_L), \tag{42}$$

where m^e is the liquidus slope in the phase diagram. Therefore the phase-field equation becomes

$$\frac{1}{M}\phi_t=\nabla\cdot\epsilon^2\nabla\phi+h'(\phi)\times\frac{RT(1-k^e)}{v_m m^e}(T_m-T-m^e c_L)-wg'(\phi). \tag{43}$$

A set of equations (20), (40), (41), and (43) is identical with the governing equations in the Steinbach and co-workers model for binary alloy solidification. Therefore the present model may be regarded as an extension of their model because the present model can be reduced to their model at a special case.

C. Equilibrium properties and parameters

Here we find the equilibrium composition, the phase field profile and the relationships between material properties and phase field parameters in the present PFM, Eqs. (31) and (32) together with auxiliary equations (20), (21), and (29). At 1D stationary state, Eq. (32) yields $f^L_{c_L}(c_L)=f^e_c$ (constant). According to the condition (21), therefore, we get

$$f^L_{c_L}(c_L)=f^S_{c_S}(c_S)=f^e_c, \tag{44}$$

from which we can see $c_L(x)=c^e_L$ and $c_S(x)=c^e_S$. Thus the phase-field equation (31) at the equilibrium state becomes

$$\epsilon^2\frac{d^2\phi_0}{dx^2}+h'(\phi_0)[f^L(c^e_L)-f^S(c^e_S)-(c^e_L-c^e_S)f^L_{c_L}(c^e_L)]-wg'(\phi_0)=0, \tag{45}$$

where ϕ_0 is the phase-field profile at the equilibrium state. After multiplying $d\phi_0/dx$ on both side of Eq. (45) and integrating it from $x=-\infty$ to $x=+\infty$,

$$f^L(c^e_L)-f^S(c^e_S)-(c^e_L-c^e_S)f^L_{c_L}(c^e_L)=0. \tag{46}$$

Equations (44) and (46) result in the well-known equilibrium condition

$$f^S_{c_S}(c^e_S)=f^L_{c_L}(c^e_L)=\frac{f^L(c^e_L)-f^S(c^e_S)}{c^e_L-c^e_S}, \tag{47}$$

by which the equilibrium compositions of solid and liquid can be determined at a given temperature.

By using Eq. (46), the phase field equation (45) at the equilibrium state reduces to

$$\epsilon^2 \frac{d^2\phi_0}{dx^2} = w \frac{dg(\phi_0)}{d\phi_0}. \tag{48}$$

With $g(\phi)=\phi^2(1-\phi)^2$, under the conditions of $\phi_0=1$(solid) at $x\rightarrow-\infty$ and $\phi_0=0$ (liquid) at $x\rightarrow+\infty$, the equilibrium phase-field profile is given by

$$\phi_0(x)=\frac{1}{2}\left[1-\tanh\left(\frac{\sqrt{w}}{\sqrt{2}\epsilon}x\right)\right]. \tag{49}$$

Using Eq. (20), then the equilibrium concentration profile is

$$c_0(x)=h(\phi_0(x))c_S^e+\{1-h[\phi_0(x)]\}c_L^e. \tag{50}$$

By considering the free energy functional corresponding to the original equations (18) and (19), it can be easily shown that the interface energy σ is given by

$$\sigma=\epsilon^2\int_{-\infty}^{+\infty}\left(\frac{d\phi_0}{dx}\right)^2 dx. \tag{51}$$

Using Eq. (49), direct evaluation of the interface energy σ and interface thickness 2λ gives

$$\sigma=\frac{\epsilon\sqrt{w}}{3\sqrt{2}}, \tag{52}$$

$$2\lambda=\alpha\sqrt{2}\,\frac{\epsilon}{\sqrt{w}}, \tag{53}$$

where α is a constant which is dependent on the definition of the interface thickness, e.g. $\alpha\simeq2.2$ when ϕ_0 changes from 0.1 to 0.9 at $-\lambda<x<\lambda$, and $\alpha\simeq2.94$ when ϕ_0 changes from 0.05 to 0.95. The parameter relationships (52) and (53) are the same as those in the PFM for pure materials.

The notable difference between the present model and the WBM model lies in definition of the free energy density for interfacial region at an equilibrium state. In the WBM model [10,13], in addition to an imposed double-well potential $wg(\phi_0)$, there exists an extra double-well potential. The extra potential originates from the definition itself of the free energy density for the interfacial region, as shown in our previous paper [23]. In the WBM model, any point within the interfacial region at an equilibrium state is assumed to be a mixture of solid and liquid with a same composition $c_0^*(x)$, where $c_0^*(x)$ is the equilibrium concentration profile in the WBM model and changes continuously from c_S^e in solid to c_L^e in liquid across the interface. This situation is very similar to the formulation of the free energy for spinodal decomposition by Cahn and Hilliard [29]. Figure 1 shows the typical free energy curves (solid curves) of solid and liquid against composition. The free energy density $h(\phi_0)f^S(c_0^*)+[1-h(\phi_0)]f^L(c_0^*)$ at the interfacial region in the WBM model lies on the dotted curve in Fig. 1 and the extra potential is

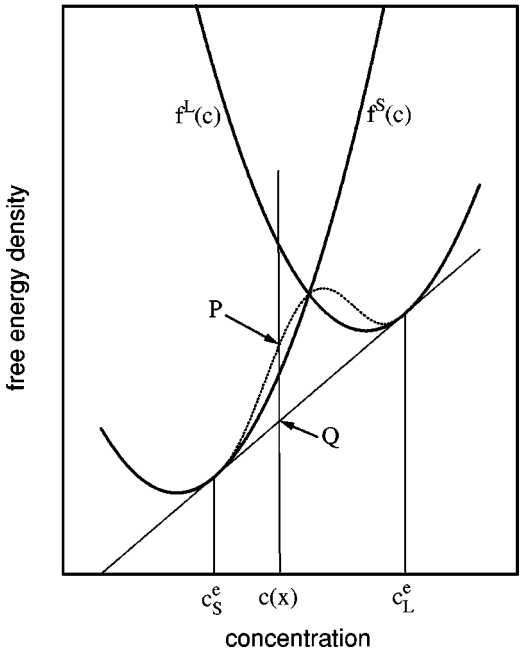

FIG. 1. Free energy densitiy curves of solid and liquid against composition.

represented by the difference (PQ) between the dotted curve (P) and the common tangent line (Q) [23], as in Cahn and Hilliard [29]. This extra potential in the WBM model may be negligible compared with $wg(\phi_0)$ either at the sharp interface limit where $w\rightarrow\infty$ or in an alloy with a very small $c_L^e-c_S^e$ where the height of the extra potential itself is very small. With increasing interface thickness or increasing $c_L^e-c_S^e$, however, the extra potential height becomes significant and cannot be ignored. In the present model, however, the interfacial region at an equilibrium state is defined as a mixture of solid and liquid with constant compositions c_S^e and c_L^e, respectively. The composition and the free energy density without the imposed potential $\omega g(\phi)$ at a certain point x within the interfacial region are given by the fraction-weighted average values $h(\phi_0)c_S^e+[1-h(\phi_0)]c_L^e$ and $h(\phi_0)f^S(c_S^e)+[1-h(\phi_0)]f^L(c_L^e)$, respectively. Thus the extra potential in the WBM model does not appear in the present model because the free energy $h(\phi_0)f^S(c_S^e)+[1-h(\phi_0)]f^L(c_L^e)$ corresponds to the common tangent line itself.

III. THIN-INTERFACE LIMIT

In this section we focus on the relationship between the phase field mobility and the interface kinetics coefficient, which is a proportional constant between the driving force of solidification and interface moving velocity. The driving force of solidification without the solute-drag effect [22] is given by

$$\Delta F_S=f^L(c_L^i)-f^S(c_S^i)-(c_L^i-c_S^i)f^L_{c_L}(c_L^i), \tag{54}$$

where c_L^i and c_S^i are the compositions at the liquid and solid sides of the interface respectively. With the driving force given by Eq. (54), following our previous work [23] on the WBM model, one can find a relationship between the inter-

face kinetics coefficient and the phase-field mobility in the present model. However, there is another useful relationship, which can correlate PFM for solidification with classical sharp interface solidification model and its local equilibrium condition. Such a relationship was first derived by Karma and Rappel [25] for a PFM of a pure material solidification. They showed that a relationship could be found at a thin-interface limit where the interface thickness is small compared with the diffusive boundary layer. In this section, under an assumption of negligible diffusivity in solid, we will derive a corresponding relationship for the present alloy PFM at a thin-interface limit condition. At 1D instantaneous steady state, the governing equations (31) and (32) become

$$-\frac{V}{M}\frac{d\phi}{dx}=\epsilon^2\frac{d^2\phi}{dx^2}+h'(\phi)[f^L(c_L)-f^S(c_S)-(c_L-c_S)f^L_{c_L}(c_L)]-wg'(\phi), \tag{55}$$

$$-V\frac{dc}{dx}=\frac{d}{dx}\left[\frac{D(\phi)}{f_{cc}}\frac{d}{dx}f^L_{c_L}(c_L)\right]. \tag{56}$$

When the diffusivity in solid is negligible, integrating Eq. (56) gives the chemical potential profile across the interface

$$f^L_{c_L}[c_L(x)]=f^S_{c_S}(c^i_S)-V\int_{-\lambda}^{x}\frac{f_{cc}}{D(\phi)}[c(x)-c^i_S]dx, \tag{57}$$

where c^i_S is the composition at the solid side ($x=-\lambda$) of the interface and f_{cc} is given by Eq. (29). To the first oder in the Péclet number, $P=2\lambda V/\tilde{D}$ ($\tilde{D}$: average interface diffusivity), the chemical potential profile $f_c(x)$ can be written as

$$f^L_{c_L}[c_L(x)]=f^S_{c_S}(c^i_S)-V\int_{-\lambda}^{x}\frac{f^e_{cc}}{D(\phi_0)}[c_0(x)-c^e_S]dx, \tag{58}$$

where $f^e_{cc}=f_{cc}(c^e_S,c^e_L,\phi_0)$. We expand $c_L(x)$ and $c_S(x)$ in the bracket of Eq. (55); $c_L=c^e_L+\delta c_L$ and $c_S=c^e_S+\delta c_S$. Then by using Eq. (46) it can be shown that

$$f^L(c_L)-f^S(c_S)-(c_L-c_S)f^L_{c_L}(c_L)=f^L(c^e_L)-f^S(c^e_S)-(c^e_L-c^e_S)f^L_{c_L}(c_L), \tag{59}$$

to the first oder in P. We insert Eqs. (58) and (59) into Eq. (55), and after multiplying $d\phi/dx$ on both sides of Eq. (55) we integrate from $x=-\lambda$ to $x=+\lambda$, which yields

$$\frac{V}{M}\int_{-\lambda}^{+\lambda}\left(\frac{d\phi_0}{dx}\right)^2dx=f^L(c^e_L)-f^S(c^e_S)-(c^e_L-c^e_S)f^S_{c_S}(c^i_S)-\frac{V}{D_i}(c^e_L-c^e_S)\int_1^0\left(\int_{-\lambda}^{x}[c_0(x')-c^e_S]f^e_{cc}dx'\right)h'(\phi_0)d\phi_0, \tag{60}$$

where only for convenience we assumed a constant diffusivity D_i within the interfacial region. Using Eq. (50) for $c_0(x)$, Eq. (29) for f^e_{cc}, Eq. (51) for the interface energy and a relationship

$$\frac{dx}{d\phi_0}=-\frac{\epsilon}{\sqrt{2w}}\frac{1}{\phi_0(1-\phi_0)}, \tag{61}$$

which can be obtained from Eq. (48), it follows that

$$f^L(c^e_L)-f^S(c^e_S)-(c^e_L-c^e_S)f^S_{c_S}(c^i_S)=V\left[\frac{\sigma}{M\epsilon^2}-\frac{\epsilon}{D_i\sqrt{2w}}\zeta(c^e_S,c^e_L)\right], \tag{62}$$

where $\zeta(c^e_S,c^e_L)$ is a temperature dependent function defined by

$$\zeta(c^e_S,c^e_L)\equiv f^S_{cc}(c^e_S)f^L_{cc}(c^e_L)(c^e_L-c^e_S)^2\times\int_0^1\frac{h(\phi_0)[1-h(\phi_0)]}{[1-h(\phi_0)]f^S_{cc}(c^e_S)+h(\phi_0)f^L_{cc}(c^e_L)}\times\frac{d\phi_0}{\phi_0(1-\phi_0)}. \tag{63}$$

Equation (62) may be written as

$$(c^e_L-c^e_S)[f^e_c-f^S_{c_S}(c^i_S)]=\alpha V, \tag{64}$$

where $\alpha=\sigma/(M\epsilon^2)-\epsilon\zeta(c^e_S,c^e_L)/(D_i\sqrt{2w})$. With a dilute solution approximation, it can be shown that

$$f^e_c-f^S_{c_S}(c^i_S)\simeq\frac{RT}{v_m}\left(1-\frac{c^i_S}{c^e_S}\right), \tag{65}$$

when c^i_S is close to c^e_S at a small interfacial Péclet number. Thus Eq. (64) gives

$$T=T_m-m^e\frac{c^i_S}{k^e}-V\frac{v_m}{RT}\frac{m^e\alpha}{1-k^e}. \tag{66}$$

If we define the kinetics coefficient as

$$\beta\equiv\frac{v_m}{RT}\frac{m^e\alpha}{1-k^e}=\frac{v_m}{RT}\frac{m^e}{1-k^e}\left[\frac{\sigma}{M\epsilon^2}-\frac{\epsilon}{D_i\sqrt{2w}}\zeta(c^e_S,c^e_L)\right], \tag{67}$$

then Eq. (66) recovers the relationship in the classical sharp-interface model between the temperature and the interfacial composition:

$$T=T_m-m^e\frac{c^i_S}{k^e}-\beta V. \tag{68}$$

Equation (67) permits a vanishing kinetic coefficient by adjusting the parameters to cancel out two terms in the brackets, as in the thin-interface PFM for a pure material [25]. Note that Eq. (67) is reduced to the relationship at the sharp-interface limit condition if we take $\lambda\sim\epsilon/\sqrt{w}\rightarrow 0$.

IV. SOLUTE TRAPPING

The solute trapping occurs when the chemical potential gradient exists across the diffuse interface [26–28]. The equality (21) of the chemical potentials looks as though it will prohibit the gradient across the interface. As mentioned previously in Sec. II, the chemical potential varies across the moving interface depending on the position because the chemical potentials in Eq. (21) are values only at the same position. Therefore the solute trapping phenomenon is not excluded in the present model when the interface velocity is enough high.

In this section we show that present model correctly describes the solute trapping phenomena at a high interface velocity and compare the calculated partition coefficient with those predicted from the high velocity asymptotics of the WBM model [22]. Throughout this section we assume a dilute alloy, a constant diffusivity D_i in both the interfacial region and liquid, and negligible diffusivity in solid.

Integrating the diffusion equation (56) at a 1D steady state gives

$$\frac{d}{dx} f^L_{c_L}(c_L) = -\frac{V}{D_i}(c - c^i_S) f_{cc}. \tag{69}$$

For a dilute alloy with $(1-c_L)\to 1$ and $(1-c_S)\to 1$, it follows that

$$\frac{d}{dx} f^L_{c_L}(c_L) = f^L_{cc}(c_L)\frac{dc_L}{dx} \simeq \frac{RT}{v_m}\frac{1}{c_L}\frac{dc_L}{dx}, \tag{70}$$

$$\frac{c_S(x)}{c_L(x)} \simeq \frac{c^e_S}{c^e_L} = k^e, \tag{71}$$

where the second equation is the dilute approximation of the condition (21). Then we can write

$$c(x) \simeq [1-(1-k^e)h(\phi)]c_L(x), \tag{72}$$

$$f_{cc} \simeq \frac{RT}{v_m[1-(1-k^e)h(\phi)]c_L}. \tag{73}$$

Therefore Eq. (69) becomes

$$\frac{dc_L}{dx} + \frac{V}{D_i}c_L = \frac{V}{D_i}\frac{c^i_S}{1-(1-k^e)h(\phi)}. \tag{74}$$

Under a boundary condition $c_L = c_S/k^e = c^i_S/k^e$ at $x=-\lambda$, the solution of this equation is

$$c_L(x) = \frac{c^i_S}{k^e}e^{-V(x+\lambda)/D_i} + \frac{V}{D_i}c^i_S e^{-Vx/D_i} \times \int_{-\lambda}^{x} \frac{e^{Vx'/D_i}}{1-(1-k^e)h(\phi)}dx'. \tag{75}$$

In the sharp interface limit ($\lambda\to 0$) or the thin interface limit ($\lambda \ll D_i/V$), it can be easily shown that $c_L(x)$ at $x \gg \lambda$ converges to the following solution obtained in the classical sharp-interface model with the same diffusivity in liquid as D_i:

$$c_L(x) = c^i_S - c^i_S\left(1-\frac{1}{k^e}\right)e^{-Vx/D_i}, \tag{76}$$

as expected. From Eqs. (72) and (75), the concentration profile $c(x)$ across the interface is given by

$$c(x) = [1-(1-k^e)h(\phi)]\left[\frac{c^i_S}{k^e}e^{-V(x+\lambda)/D_i} + \frac{V}{D_i}c^i_S e^{-Vx/D_i}\int_{-\lambda}^{x}\frac{e^{Vx'/D_i}}{1-(1-k^e)h(\phi)}dx'\right]. \tag{77}$$

This equation yields the partition coefficient as a function of the interface velocity. The partition coefficient may be defined by following two different ways: One is the ratio of the composition at the solid side of the interface (that is, c^i_S) to the maximum composition across the interface, which has been used by Ahmad *et al.* [22]. The other is the ratio of the composition c^i_S at the solid side of the interface to the composition $c(\lambda)$ at the liquid side of the interface. When we follow the latter definition, the partition coefficient $k = c^i_S/c(\lambda)$ at a given interface velocity and phase-field profile can be directly read from Eq. (77). In this case, it can be shown that $k\to k^e$ at $V\to 0$ and $k\to 1$ at $V\to\infty$, as expected in the standard solute trapping model. In both definitions, the partition coefficient as a function of the interface velocity can be found only if the phase-field profile across the interface is known. In principle, the phase-field profile as a function of interface velocity can be obtained by solving the phase-field equation. However, Eq. (77) was derived from only diffusion equation (56) by introducing a phase field only for mathematical convenience. It may be useful to survey the solute trapping behavior for any assumed phase-field profile at $-\lambda < x < \lambda$.

By using the partition coefficient defined by Ahmad *et al.* [22], here we survey the solute trapping behavior as a function of V for a given k^e. To do this we rewrite Eq. (77) into a dimensionless form

$$\tilde{c} = [1-(1-k^e)h(\phi)]\left[\frac{1}{k^e}e^{-P(\tilde{x}+1/2)} + Pe^{-P\tilde{x}}\int_{-1/2}^{\tilde{x}}\frac{e^{P\tilde{x}'}}{1-(1-k^e)h(\phi)}d\tilde{x}'\right], \tag{78}$$

where $\tilde{x} = x/2\lambda$ and $\tilde{c} = c/c^i_S$. Therefore the relative concentration profile $\tilde{c}$, and therefore k, is governed by the interfacial Péclet number P, the equilibrium partition coefficient k^e, and the phase-field profile. We calculated the partition coefficient $k = 1/\tilde{c}_{\max}$ by numerical integration of Eq. (78) with the assumption that the phase-field profile remains unchanged from the stationary profile $\phi_0(x)$, that is,

$$\phi(\tilde{x}) = \phi_0(\tilde{x}) = \frac{1}{2}[1-\tanh(\alpha\tilde{x})], \tag{79}$$

in a dimensionless form. And we adopted $h(\phi) = \phi^2(3-2\phi)$ and $\alpha = 2.94$ with which ϕ changes from 0.05 to 0.95 at $-\lambda < x < \lambda$. Figure 2 shows the variations of concentration

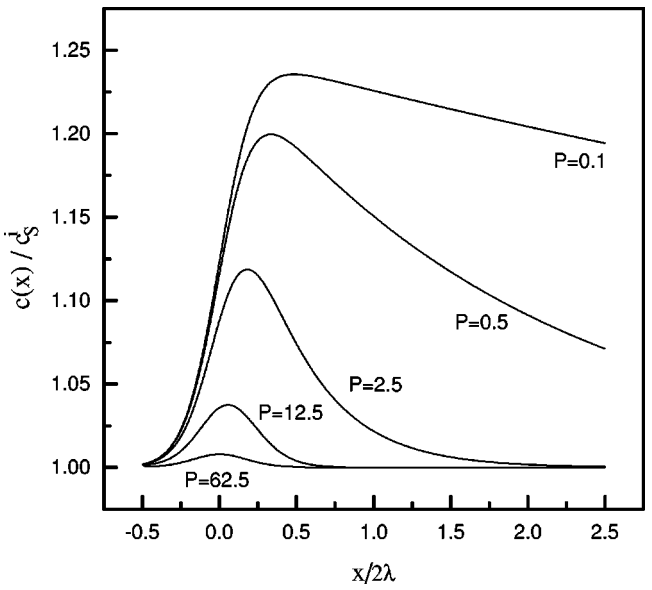

FIG. 2. Variations of concentration profiles $c(x)/c_S^i$, calculated at $k^e=0.8$ and several different values of P, where c_S^i is the solid composition at the interface and 2λ is the interface thickness.

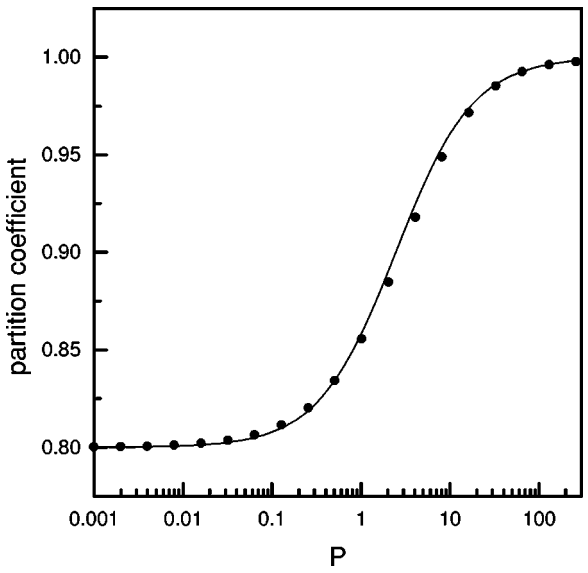

FIG. 3. Variations of the partition coefficient as a function of interfacial Péclet number P, where the filled circles are the prediction from Eq. (78) and the solid curve from the WBM's high velocity asymptotics with a constant diffusivity at the interfacial region.

profiles $\tilde{c}$ calculated at $k^e=0.8$ and several different values of P. For a low P, $c_{\max}/c_S^i$ is close to the equilibrium value 1.25, and with increasing P the height of concentration spike around the interface and thickness of diffusive boundary layer decreases as expected. Figure 3 shows variations of the partition coefficient as a function of P, where the filled circles are prediction from Eq. (78) and the solid curve from the high velocity asymptotics of the WBM model [22] with a constant diffusivity at the interfacial region, which with our definition of interface thickness can be written as

$$k(P)=\frac{k^e+\gamma P}{1+\gamma P}, \tag{80}$$

where

$$\gamma=\frac{8(1-k^e)}{6\alpha\ln(1/k^e)}. \tag{81}$$

The partition coefficient curves from Eq. (78) and the high velocity asymptotics of the WBM model appear to be nearly identical. With decreasing k^e, the partition coefficient curve from Eq. (78) moved significantly to the high P direction, which has also been observed in the high velocity asymptotics of the WBM model [22]. A detailed analysis of the partition coefficient in the present model and a comparison with the reported experimental results will appear elsewhere [31].

One interesting situation is the case with the complete solute trapping, that is, partitionless solidification. For partitionless solidification the interface temperature T should be lower than T_0 temperature where the free energy densities of solid and liquid become equal. For a dilute solution, the condition can be written as [22]

$$T<T_0=T_m+c_\infty\frac{m^e\ln k^e}{1-k^e}, \tag{82}$$

where c_∞ is the bulk composition. The interface velocity during the partitionless solidification is given by $(T_0-T)/\beta$ [22]. Here we will derive similar result from the present alloy PFM. For a dilute solution the phase-field equation in a 1D steady state is

$$-\frac{V}{M}\frac{d\phi}{dx}=\epsilon^2\frac{d^2\phi}{dx^2}+h'(\phi)\frac{RT}{v_m}[(c_L^e-c_S^e)-(c_L-c_S)]-wg'(\phi). \tag{83}$$

Also, for the partitionless solidification, Eq. (72) yields

$$c_L=\frac{c_\infty}{1-(1-k^e)h(\phi)}. \tag{84}$$

With the approximation (71) for a dilute solution, we can get

$$-\frac{Vv_m}{MRT}\frac{d\phi}{dx}=\epsilon^2\frac{d^2\phi}{dx^2}+h'(\phi)(1-k^e)c_L^e+c_\infty\frac{d}{d\phi}\ln[1-(1-k^e)h(\phi)]-wg'(\phi). \tag{85}$$

After multiplying $d\phi/dx$ on both sides of Eq. (85), we integrate from $x=-\infty$ to $x=+\infty$, which yields a solvability condition

$$\frac{Vv_m}{MRT}\int_{-\infty}^{+\infty}\left(\frac{d\phi}{dx}\right)^2dx=(1-k^e)c_L^e+c_\infty\ln k^e. \tag{86}$$

Therefore, the condition required for the partitionless solidification $(V>0)$ is given by

$$(1-k^e)c_L^e+c_\infty\ln k^e>0, \tag{87}$$

which is identical with Eq. (82) because $c_L^e=(T_m-T)/m^e$. Also if $\phi(x)\simeq\phi_0(x)$, then Eq. (86) can be written in the form $(T_0-T)=\beta V$, where

$$\beta=\frac{v_m}{RT}\frac{m^e}{1-k^e}\frac{\sigma}{M\epsilon^2}, \tag{88}$$

which is the same relationship as that at the sharp-interface limit condition, that is, Eq. (67) with $\lambda\sim\epsilon/\sqrt{w}\to 0$. Thus the sharp interface PFM yields the correct interface velocity for the partitionless solidification.

V. NUMERICAL SIMULATION

For 1D steady state solidification, the classical sharp interface model can be exactly soluble. We solve numerically the present alloy PFM for 1D steady state solidification at those situations and compare the calculated results with the exact solutions.

The 1D isothermal system initially has an uniform bulk composition c_∞ and a temperature with a given undercooling. A solid phase starts to grow from one end of the system. The system can reach a steady state either when the system temperature is lower than the solidus or when there exists a solute sink in liquid, engulfing all solute influx from its neighbor, even if the system temperature is between solidus and liquidus temperatures. In the latter case which was adopted in our previous work [23] for steady-state simulations, the solute sink continuously move with the same instantaneous velocity as the interface, maintaining a prescribed distance from the moving interface. In the classical sharp-interface model with diffusion in liquid only, both situations can be described by

$$-V\frac{dc}{dx}=D_L\frac{d^2c}{dx^2}, \tag{89}$$

$$V(1-k^e)c^i=-D_L\left(\frac{dc}{dx}\right)_i, \tag{90}$$

$$T=T_m-m^ec^i-\beta V, \tag{91}$$

$$c(\xi^*)=c_\infty, \tag{92}$$

where ξ^* is the prescribed distance between the interface and the solute sink in liquid, and c^i is the composition at the interface. The case with $\xi^*\to\infty$ corresponds to the former situation and the case with a finite ξ^* corresponds to the latter situation. The exact solution of the concentration profile in Eqs. (89)–(92) is

$$c(x)=c_\infty+c_\infty\frac{(1-k^e)(e^{-Vx/D_L}-e^{-V\xi^*/D_L})}{1-(1-k^e)(1-e^{-V\xi^*/D_L})}. \tag{93}$$

Then the interface velocity is determined from

$$\beta V=T_m-T-\frac{m^ec_\infty}{1-(1-k^e)(1-e^{-V\xi^*/D_L})}. \tag{94}$$

When $\xi^*\to\infty$, Eq. (94) shows that a positive interface velocity is guaranteed only when the temperature T is lower than the solidus temperature $T_{\rm sol}=T_m-m^ec_\infty/k^e$. When ξ^* takes a finite value, on the other hand, there exists a positive velocity satisfying Eq. (94) whenever the temperature is lower than the liquidus temperature $T_{\rm liq}=T_m-m^ec_\infty$. It should be mentioned that in the case with a finite ξ^* there exists an unique positive velocity in Eq. (94) even when $\beta=0$, which enables us to test the condition for the vanishing interface kinetics coefficient at the thin-interface limit. We will compare the exact solution (94) with the results obtained from numerical calculation of our PFM at above two different situations, that is, with and without a solute sink in liquid.

Another situation where the exact analytic solution is available is the case of the partitionless solidification. In this case, we showed in Sec. IV that the present PFM yields the interface velocity $V=(T_0-T)/\beta$. This point will also be tested.

For computational works, we used the dilute solution version of our model; Eqs. (20), (34), (38), and (39) with $h(\phi)=\phi^2(3-2\phi)$. The steady-state solution was found by observing the long time behavior of the full dynamic equations. The detailed numerical procedure is similar to that used in the previous work [23]. The model system was selected to be a Ni-Cu (0.05 mole fraction) alloy, which was regarded as a dilute solution rather than an ideal solution. The material parameters used for computation are as follows: $D_S=1\times10^{-14}$ m^2/s, $D_L=1\times10^{-9}$ m^2/s, $T_m=1728.0$ K, $m^e=310.9$ K, $k^e=0.7965$, $\sigma=0.37$ J/m^2, $\beta=10$ K s/m. These data yield the liquidus and solidus temperatures of $T_{\rm liq}=1712.5$ and $T_{\rm sol}=1708.5$, respectively. The grid size Δx was 1 nm and the interface thickness 2λ over where the phase field changes from 0.05 to 0.95 was taken as $8\Delta x$. Within the interfacial region, the diffusivity D_i was taken as the same value as D_L. With these parameters, two kinds of computations were performed. In the first series, we took $\beta=10$ K s/m and $\xi^*\to\infty$ and measured the interface velocities at various levels of undercooling below the solidus temperature. In this series, both the thin interface and sharp interface PFMs were compared with each other. The second series of computation was performed at a constant temperature (1709 K) to test the condition for vanishing kinetics coefficient at the thin-interface PFM. In this series, we set the parameters to yield $\beta=0$ in Eq. (67) and measured the interface velocity and the solid compositions at various ξ^* values. The function $\zeta(c_S^e,c_L^e)$ of Eq. (67) required for the thin-interface PFM was calculated from the dilute solution approximation of Eq. (63):

$$\zeta(c_S^e,c_L^e)=\frac{RT}{v_m}(c_L^e-c_S^e)^2\int_0^1\frac{\phi(1-\phi)(3-2\phi)(2\phi+1)}{(1-\phi)^2(2\phi+1)c_L^e(1-c_L^e)+\phi^2(3-2\phi)c_S^e(1-c_S^e)}d\phi, \tag{95}$$

as a function of temperature, where we used $h(\phi)=\phi^2(3-2\phi)$.

Figure 3 shows variations of the steady-state interface velocity, calculated from the case without solute sink ($\xi^*\rightarrow\infty$), as a function of undercooling $T_{sol}-T$. The solid straight line is the analytic solution (94) of the classical sharp-interface model, the dotted line is the analytic solution for the partitionless solidification $V=(T_0-T)/\beta$, the filled circles and the crosses are the calculated results from the thin-interface PFM and the sharp-interface PFM, respectively. The interface velocity from the sharp-interface PFM deviates from the analytic solution by a constant ratio, independent of the undercooling. On the other hand, the interface velocity from the thin-interface PFM converges to the analytic solution as the undercooling decreases. The deviation at high interface velocity is because the thin-interface limit was derived at the low Péclet number condition. At undercoolings close to 10 K, the height of the concentration spike across the interface appeared to be negligible in both the PFMs, which may be regarded as the partitionless solidification. As seen in Fig. 4, the interface velocity from the sharp-interface PFM approaches the analytic solution for the partitionless solidification at large undercooling, as expected in Sec. IV.

Figure 5 shows variations of steady state interface velocity, calculated without kinetic effect ($\beta=0$), as a function of distance ξ^* between interface and solute sink. The system temperature was 1709 K which is between the solidus and liquidus temperatures. The curved line is the analytic solution (94) for the classical sharp-interface model and the filled circles are the calculated results from the thin-interface PFM with vanishing kinetics coefficient. Two results are in excellent agreement with each other. The error in interface velocity was within 2 % for $\xi^*>40\Delta x$. In order to see in detail the situation of the vanishing kinetics effect, we checked the solid compositions with varying ξ^*, which is shown in Fig. 6. The vertical axis represents the relative difference between the measured solid composition and the equilibrium composition, scaled by the equilibrium composition (c_S^e). The deviation of the solid composition at $\xi^*>40\Delta x$ from the equilibrium composition is within 0.06%. Owing to the vanishing interface kinetics condition in the thin-interface PFM, the solid composition stays at the equilibrium value, in other words, local equilibrium state is maintained at the interface without kinetic undercooling. The physical meaning of the vanishing kinetics condition in the thin-interface alloy PFM may be interpreted as follows: A finite phase-field mobility decreases the solid composition [10,23]. On the other hand, the finite interface thickness bringing the solute trapping effect increases the solid composition [22,23]. At the condition where two opposing effects are exactly cancelled out, the solid composition recovers the equilibrium composition, which is the condition for vanishing kinetics coefficient in the thin-interface PFM.

Until now our numerical simulations were presented only for a dilute alloy. In dendritic simulations of nondilute alloys, there are some complexities related with the condition (21) of the equal chemical potentials in solving a set of equations (20), (21), (31), and (32) or equations (20), (21), (31), and (33). Let us suppose that all the values of c_S^n, c_L^n, c^n, and ϕ^n in current nth time step are given. In the next $(n+1)$th time step we can calculate c^{n+1} and ϕ^{n+1} from Eqs. (31) and (33) and by using them we should find c_S^{n+1} and

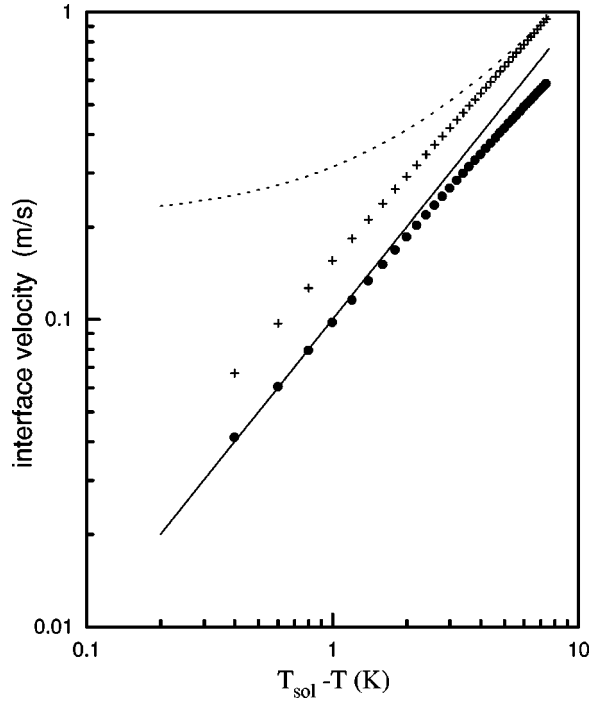

FIG. 4. Variations of steady state interface velocity, calculated at $\xi^*\rightarrow\infty$, as a function of undercooling $T_{sol}-T$. The solid straight line is the analytic solution (94) of the classical sharp-interface model, the dotted line is the analytic solution for the partitionless solidification $V=(T_0-T)/\beta$, and the filled circles and the crosses are the calculated results from the thin-interface PFM and the sharp-interface PFM, respectively.

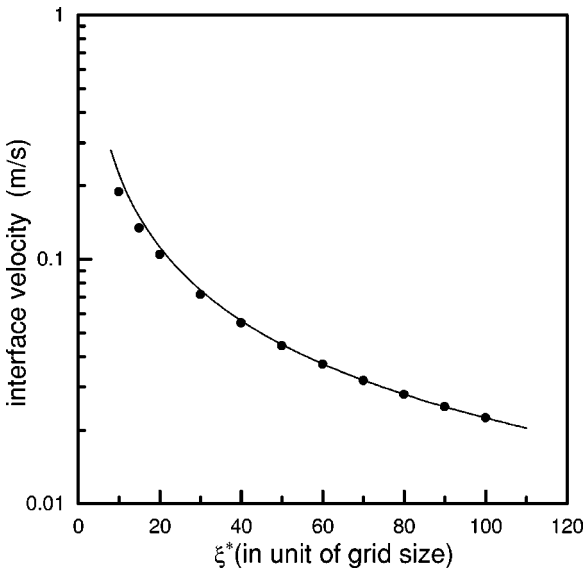

FIG. 5. Variations of interface velocity, calculated without kinetic effect ($\beta=0$), as a function of distance ξ^* between the interface and a solute sink in liquid, which engulfs all solute influx from its neighbor. The system temperature is 1709 K which is between the solidus and liquidus temperatures. The curved line is the analytic solution (94) for the classical sharp-interface model and the filled circles are the calculated results from the thin-interface PFM with vanishing kinetics coefficient.

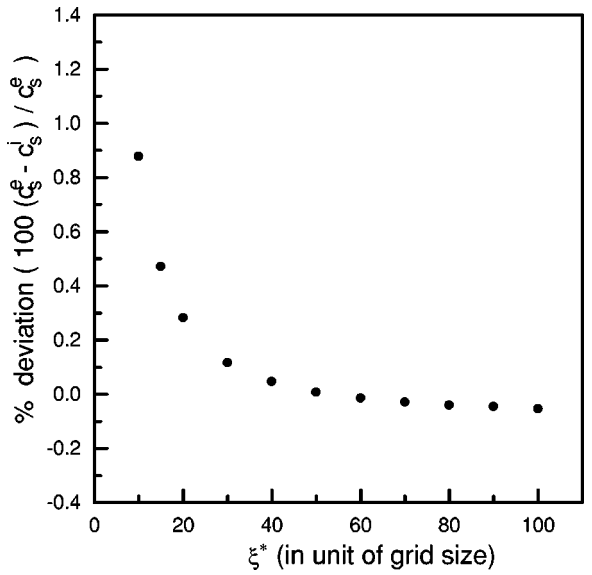

FIG. 6. Variation of solid composition with ξ^* values calculated by the thin-interface PFM model with vanishing kinetics coefficient. The vertical axis represents the relative solid composition scaled by the equilibrium composition (c_S^e).

c_L^{n+1} from Eqs. (20) and (21). This last step is a very time-consuming iteration procedure because one should work with complex thermodynamic data. Futhermore, when the solubility in solid is low, the iteration may not converge because the chemical potential becomes infinite as $c_S \rightarrow 0$. These serious problems, especially in two-dimensional simulations, can be tackled as follows: Before the simulation, the thermodynamic data given by the free energies of the related phases as functions of compositions are transformed into the compositions as functions of the chemical potentials. The compositions c_S and c_L may be expressed by power series of the chemical potentials $f_{c_S}^S = f_{c_L}^L = f_c$ or by tables. With the calculated c^{n+1} and ϕ^{n+1}, now we can find chemical potential f_c^{n+1} from Eq. (20) by the Newton-Raphson method, where the iteration procedure is very efficient: The errors in compositions after only three iterations were less then 10^{-4}% in general. Then the compositions c_s^{n+1} and c_L^{n+1} can be directly read from the predetermined relationship between compositions and chemical potentials. Note that we do not solve Eq. (21) because it is automatically satisfied in the above procedure. Indeed we have simulated the dendritic growth during two-dimensional isothermal solidification of nondilute Al-Cu alloys by using published thermodynamic data [29,30]. The calculation time was increased by only about 10%, when compared with the simulation using the dilute solution approximation where the iteration is not needed because Eqs. (20) and (21) are reduced to a quadratic equation for c_S^{n+1} or c_L^{n+1}.

VI. CONCLUSION

We presented a PFM for solidification in binary alloys, which was found from the PFM for pure material by direct comparison of the variables for a pure material solidification and alloy solidification. The model appears to be equivalent to the WBM model but has a different definition of the free energy density for the interfacial region. An extra potential originated from the free energy density definition in the WBM model disappears in this model. At the dilute solution limit, the model is reduced to the Steinbach and co-workers model.

A relationship between the phase-field mobility and the interface kinetics coefficient was derived at a thin-interface limit condition under an assumption of negligible diffusivity in solid phase. The effect of a finite phase-field mobility tends to decrease the solid composition and the effect of finite interface thickness increases the solid composition. At the condition with a vanishing kinetics coefficient, both effects are exactly cancelled out resulting in maintenance of local equilibrium at the interface. For a dilute alloy, a steady-state solution of the concentration profile across the diffuse interface was obtained as a function of the interface velocity and the resultant partition coefficient appears to be nearly identical with that from the WBM model.

For the 1D steady state alloy solidification, we performed numerical simulations of the phase-field model at the situations where the classical sharp-interface model is exactly soluble: At low interface velocities, the simulated results from the thin-interface PFM were in excellent agreement with the exact solutions. As the partition coefficient becomes close to unity at high interface velocities, whereas, the interface velocity from the sharp-interface PFM converged to that given by the standard model for partitionless solidification, as predicted.

ACKNOWLEDGMENT

One of us (W.T.K.) thanks Creative Research Initiatives of the Korean Ministry of Science and Technology for support.

[1] J. S. Langer, in *Directions in Condensed Matter* (World Scientific, Singapore, 1986), p. 164.
[2] J. B. Collins and H. Levine, Phys. Rev. B **31**, 6119 (1985).
[3] G. Caginalp, Phys. Rev. A **39**, 5887 (1989).
[4] R. Kobayashi, Physica D **63**, 3410 (1993).
[5] G. B. McFadden, A. A. Wheeler, R. J. Braun, S. R. Coriell, and R. F. Sekerka, Phys. Rev. E **48**, 2016 (1993).
[6] A. A. Wheeler, B. T. Murray, and R. J. Schaefer, Physica D **66**, 243 (1993).
[7] S.-L. Wang and R. F. Sekerka, Phys. Rev. E **53**, 3760 (1996).
[8] O. Penrose and P. C. Pife, Physica D **43**, 44 (1990).
[9] S.-L. Wang, R. F. Sekerka, A. A. Wheeler, B. T. Murray, S. R. Coriell, R. J. Braun, and G. B. McFadden, Physica D **69**, 189 (1993).
[10] A. A. Wheeler, W. J. Boettinger, and G. B. McFadden, Phys. Rev. A **45**, 7424 (1992).
[11] A. A. Wheeler, W. J. Boettinger, and G. B. McFadden, Phys. Rev. E **47**, 1893 (1993).
[12] A. Karma, Phys. Rev. E **49**, 2245 (1994).
[13] A. A. Wheeler, G. B. McFadden, and J. B. Boettinger, Proc. R.

Soc. London, Ser. A **452**, 495 (1996).
[14] K. R. Elder, F. Drolet, J. M. Kosterlitz, and M. Grant, Phys. Rev. Lett. **72**, 677 (1994).
[15] J. A. Warren and W. J. Boettinger, Acta Metall. Mater. **43**, 689 (1995).
[16] G. Caginalp and W. Xie, Phys. Rev. E **48**, 1897 (1993).
[17] H. I. Diepers, C. Beckermann, and I. Steinbach (unpublished).
[18] J. Tiaden, B. Nestler, H. J. Diepers, and I. Steinbach, Physica D **115**, 73 (1998).
[19] W. Losert, D. A. Stillman, H. Z. Cummins, P. Kopczyński, W. J. Rappel, and A. Karma, Phys. Rev. E **58**, 7492 (1998).
[20] H. Löwen, J. Bechhoefer, and L. S. Tuckerman, Phys. Rev. A **45**, 2399 (1992).
[21] M. Conti, Phys. Rev. E **58**, 2071 (1998).
[22] N. A. Ahmad, A. A. Wheeler, W. J. Boettinger, and G. B. McFadden, Phys. Rev. E **58**, 3436 (1998).
[23] S. G. Kim, W. T. Kim, and T. Suzuki, Phys. Rev. E **58**, 3316 (1998).
[24] J. S. Langer, Rev. Mod. Phys. **52**, 1 (1980).
[25] A. Karma and W. J. Rappel, Phys. Rev. Lett. **77**, 4050 (1996); Phys. Rev. E **53**, R3017 (1996); **57**, 4323 (1998).
[26] M. J. Aziz, J. Appl. Phys. **53**, 1158 (1982).
[27] M. J. Aziz and T. Kaplan, Acta Metall. **36**, 2335 (1988).
[28] M. J. Aziz, Metall. Mater. Trans. A **27**, 671 (1996).
[29] J. W. Cahn and J. E. Hilliard, J. Chem. Phys. **28**, 258 (1958).
[30] J. L. Murray, Int. Met. Rev. **30**, 211 (1985).
[31] S. G. Kim, W. T. Kim, and T. Suzuki (unpublished).